We are IntechOpen, the world's leading publisher of Open Access books Built by scientists, for scientists

4,800
Open access books available

122,000
International authors and editors

135M
Downloads

Our authors are among the

154
Countries delivered to

TOP 1%
most cited scientists

12.2%
Contributors from top 500 universities

WEB OF SCIENCE™

Selection of our books indexed in the Book Citation Index in Web of Science™ Core Collection (BKCI)

Interested in publishing with us?
Contact book.department@intechopen.com

Numbers displayed above are based on latest data collected.
For more information visit www.intechopen.com

24

Pseudo-Bessel Beams in Millimeter and Sub-millimeter Range

Yanzhong Yu[1,2] and Wenbin Dou[1]
[1.] *State Key Lab of Millimeter Waves, Southeast University, Nanjing,*
[2.] *School of Science, Quanzhou Normal University, Quanzhou,*
P. R. China

1. Introduction

In 1987, Durnin firstly discovered a class of novel solutions of the free-space scalar wave equation for beams that are diffraction-free (Durnin, 1987). This means that the time-averaged intensity pattern is unchanged in the cross-section when such beam propagates in free space (McGloin & Dholakia, 2005). It is Bessel beams that are the one most interesting family of diffraction-free beams. The transverse intensity distributions of ideal Bessel beams can be highly localized, and therefore they have many unique properties, such as large depth of field, propagation invariant and reconstruction (MacDonald et al., 1996; Bouchal et al., 1998) and so on. Unfortunately, the ideal Bessel beams can not be exactly generated, due to their infinite lateral extent and energy (Monk et al., 1999). Only their approximations known as the near or pseudo-Bessel beams can be obtained physically (Bouchal, 2003), but they can still propagate over extended distances in a diffraction-free manner (Arlt & Dholakia, 2000). In optics they could have prospective applications, such as optical alignment, interconnection, and promotion of free electron laser gain (Li et al., 2006), and they may be useful in power transmission, communications and imaging applications (Mahon et al., 2005) in millimeter and sub-millimeter range. Therefore, much attention has been paid to this subject, and numerous papers have been devoted to the generation and applications of Bessel beams.

More recently, the studies of Bessel beams at millimeter and sub-millimeter wavelengths have been carried out in our group. The main aim of this chapter is to present our investigation results comprehensively, including their theories, generation, propagation and potential applications. The relevant contents are organized as follows. Section 2 gives the scalar and vector analyses of Bessel Beams. How to produce pseudo-Bessel beams is described in Section 3 and 4. The comparison of propagation distance between apertured Bessel and Gaussian beams is made in Section 5. Lots of potential applications are discussed in the last Section 6.

2. Scalar and Vector Analyses of Bessel Beams (Yu & Dou, 2008a; Yu & Dou, 2008b)

2.1 Scalar analysis

In free space, the scalar field is governed by the following wave equation

$$\nabla^2 E(\vec{r},t) - \frac{1}{c^2}\frac{\partial^2}{\partial t^2} E(\vec{r},t) = 0 \tag{1}$$

where ∇^2 is the Laplacian operator, c is the velocity of light in free space, $\vec{r}$ is the position vector. Assuming that the angular frequency is ω, the field $E(\vec{r},t)$ can be written as

$$E(\vec{r},t) = E(\vec{r})\exp(-i\omega t) \tag{2}$$

Substituting (2) into (1), we have the homogeneous Helmholtz wave equation

$$\nabla^2 E(\vec{r}) + k^2 E(\vec{r}) = 0 \tag{3}$$

where $k = \omega^2 \mu_0 \varepsilon_0$, is the wave number in free space. Applying the method of separation of variables in cylindrical coordinates, we can derive the following solution from (3)

$$E(\vec{r},t) = E_0 J_n(k_\perp \rho)\exp(in\varphi)\exp(i(k_z z - \omega t)) \tag{4}$$

where E_0 is a constant, J_n is the *nth* -order Bessel function of the first kind, $\rho = \sqrt{x^2 + y^2}$, $x = \rho\cos\varphi$, $y = \rho\sin\varphi$, $k_\perp^2 + k_z^2 = k^2$, $k_\perp$ and k_z are the radial and longitudinal wave numbers, respectively. Thus the time-average intensity of (4) can be given by

$$I(\rho,\varphi,z \geq 0) = I(\rho,\varphi,z = 0) = |E_0 J_n(k_\perp \rho)|^2 \tag{5}$$

It can be seen from (5) that the intensity distribution always keeps unchanged in any plane normal to the z-axis. This is the characteristic of the so-called nondiffracting Bessel beams.

When $n = 0$, (4) represents the zero-order Bessel beams (i.e. J_0 beams) presented by Durnin in 1987 for the first time (Durnin, 1987). The central spot of a J_0 beam is always bright, as shown in Figs. 1(a) and 1(b). The size of the central spot is determined by $k_\perp$, and when $k_\perp = k$, it reaches the minimum possible diameter of about $3\lambda/4$, but when $k_\perp = 0$, (4) reduces to a plane wave. The intensity profile of a J_0 beam decays at a rate proportional to $(k_\perp \rho)^{-1}$, so it is not square integrable (Durnin, 1987). However, its phase pattern is bright-dark interphase concentric fringes, as shown in Fig. 1(c). An ideal Bessel beam extends infinitely in the radial direction and contains infinite energy, and therefore a physically generated Bessel beam is only an approximation to the ideal. Experimentally, the generation of an approximate J_0 beam is reported firstly by Durnin and co-workers (Durnin et al., 1987). The geometrical estimate of the maximum propagation rang of a J_0 beam is given by

$$Z_{\max} = R[(k/k_\perp)^2 - 1]^{1/2} \tag{6}$$

where R is the radius of the aperture in which the J_0 beam is formed. We can see from (6) that when $R \to \infty$, then $Z_{\max} \to \infty$, provided that $k/k_\perp$ is a fixed value.

But for $n > 0$, (4) denotes the high-order Bessel beams (i.e. J_n beams, n is an integer). The intensity distribution of all the higher-order Bessel beams has zero on axis surrounded by concentric rings. For example, when $n = 3$, the J_3 beam has a dark central spot and its first bright ring appears at $\rho = 4.201/k_\perp$, as illustrated in Figs. 2(a) and 2(b). However, the phase

pattern of the J_n beam is much different from that of the J_0 beam. It has $2n$ arc sections distributed evenly from the innermost to the outermost ring, as shown in Fig. 2(c).

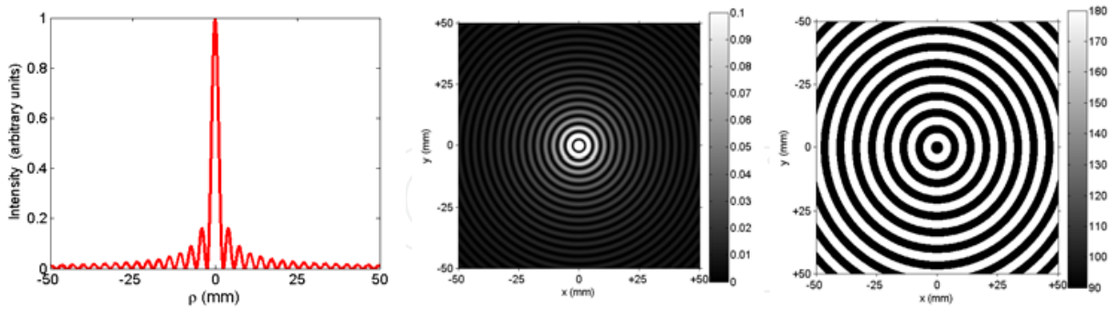

(a) (b) (c)

Fig. 1. A J_0 beam. (a) One-dimensional (1-D) intensity distribution. (b) 2-D intensity distribution plotted in a gray-level representation. (c) Phase distribution ($t=0$, $z=0$). The relevant parameters are incident wavelength of $\lambda = 3mm$, and aperture radius of $R = 50mm$, $k_\perp = 0.962mm^{-1}$.

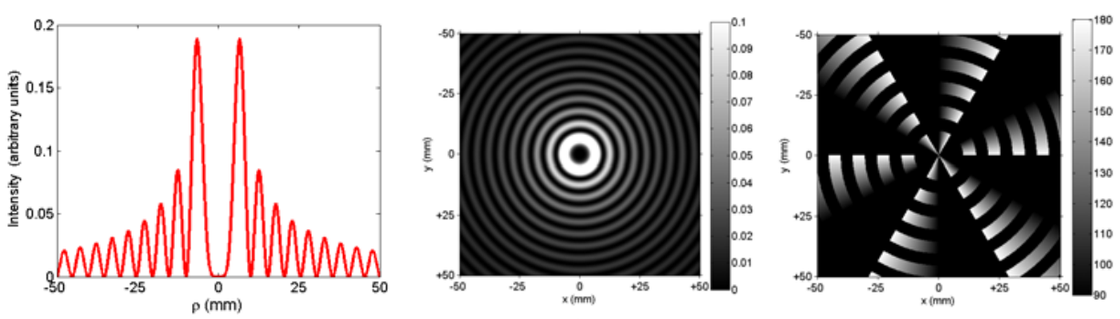

(a) (b) (c)

Fig. 2. A J_3 beam. (a) 1-D intensity distribution. (b) 2-D intensity distribution. (c) Phase distribution ($t=0$, $z=0$). The relevant parameters are the same as in Fig. 1, except $k_\perp = 0.638mm^{-1}$.

2.2 Vector analysis

2.2.1 TM and TE modes Bessel beams

In order to discover more characteristics of Bessel beams, the vector analyses should be performed. By using the Hertzian vector potentials of electric and magnetic types $\vec{\Pi}_e$, $\vec{\Pi}_m$, respectively, the fields are expressed as

$$\vec{E}_e = \nabla\times\nabla\times\vec{\Pi}_e = \nabla\nabla\bullet\vec{\Pi}_e + k^2\vec{\Pi}_e \,, \quad \vec{H}_e = i\omega_0\mu_0\nabla\times\vec{\Pi}_e \tag{7}$$

$$\vec{E}_m = -i\omega_0\mu_0\nabla\times\vec{\Pi}_m \,, \quad \vec{H}_m = \nabla\times\nabla\times\vec{\Pi}_m = \nabla\nabla\bullet\vec{\Pi}_m + k^2\vec{\Pi}_m \tag{8}$$

where $\vec{\Pi}_e$ and $\vec{\Pi}_m$ are the solutions to vector Helmholtz wave equation. In a source-free region, they satisfy the homogeneous vector Helmholtz equation, respectively. When the choice of $\vec{\Pi}_e = \Pi_e\vec{z}$ and $\vec{\Pi}_m = \Pi_m\vec{z}$, they are reduced to scalar Helmholtz equation

$$\nabla^2 \prod_e + k^2 \prod_e = 0\,, \qquad \nabla^2 \prod_m + k^2 \prod_m = 0 \tag{9}$$

From (3) and (4), we have deduced that the $\prod_e$ and $\prod_m$ can take the form of $J_n(k_\perp \rho)\exp(in\varphi)\exp(i(k_z z - \omega t))$. Thus, $\vec{\prod}_e$ and $\vec{\prod}_m$ can be written in the form

$$\vec{\prod}_e = \prod_e \vec{z} = P_e J_n(k_\perp \rho)\exp(in\varphi)\exp[i(k_z z - \omega t)]\vec{z} \tag{10a}$$

$$\vec{\prod}_m = \prod_m \vec{z} = P_m J_n(k_\perp \rho)\exp(in\varphi)\exp[i(k_z z - \omega t)]\vec{z} \tag{10b}$$

where P_e and P_m are the electric and magnetic dipole moment, respectively. By substituting (10) into (7) and (8) respectively, we finally obtain the TM and TE modes Bessel beams.

TM_n mode: TE_n mode:

$$\left.\begin{aligned}
E_{\rho e} &= iP_e k_\perp k_z J_n'(k_\perp \rho)\exp(in\varphi)\exp[i(k_z z - \omega t)] \\
E_{\varphi e} &= -\frac{n}{\rho} P_e k_z J_n(k_\perp \rho)\exp(in\varphi)\exp[i(k_z z - \omega t)] \\
E_{ze} &= P_e k_\perp^2 J_n(k_\perp \rho)\exp(in\varphi)\exp[i(k_z z - \omega t)] \\
H_{\rho e} &= \frac{n}{\rho} P_e \omega\varepsilon J_n(k_\perp \rho)\exp(in\varphi)\exp[i(k_z z - \omega t)] \\
H_{\varphi e} &= iP_e k_\perp \omega\varepsilon J_n'(k_\perp \rho)\exp(in\varphi)\exp[i(k_z z - \omega t)] \\
H_{ze} &= 0
\end{aligned}\right\} \tag{11a}$$

$$\left.\begin{aligned}
E_{\rho m} &= -\frac{n}{\rho} P_m \omega\mu J_n(k_\perp \rho)\exp(in\varphi)\exp[i(k_z z - \omega t)] \\
E_{\varphi m} &= -iP_m k_\perp \omega\mu J_n'(k_\perp \rho)\exp(in\varphi)\exp[i(k_z z - \omega t)] \\
E_{zm} &= 0 \\
H_{\rho m} &= iP_m k_\perp k_z J_n'(k_\perp \rho)\exp(in\varphi)\exp[i(k_z z - \omega t)] \\
H_{\varphi m} &= -\frac{n}{\rho} P_m k_z J_n(k_\perp \rho)\exp(in\varphi)\exp[i(k_z z - \omega t)] \\
H_{zm} &= P_m k_\perp^2 J_n(k_\perp \rho)\exp(in\varphi)\exp[i(k_z z - \omega t)]
\end{aligned}\right\} \tag{11b}$$

From (11), their instant field vectors and intensity distributions for the TM or TE modes Bessel beams can be easily obtained. Two examples for TM_0 and TE_0 modes Bessel beams are illustrated in Figs. 3 and 4, respectively. From (11a), we can see that the transverse electric field component of the TM_0 mode is only a radial part and thus it is radially polarized. This can also be seen from Fig. 3(a). Similarly, the TE_0 mode is only an azimuthal component of the electric field and thus is azimuthally polarized. Its field vectors at $t = 0$ are shown in Fig. 4(a).

2.2.2 Polarization States

To analyze the polarization states of Bessel beams, (11) in cylindrical coordinates are transformed into rectangular coordinates. Applying the relationships: $\vec{x} = \vec{\rho}\cos\varphi - \vec{\varphi}\sin\varphi$, and $\vec{y} = \vec{\rho}\sin\varphi + \vec{\varphi}\cos\varphi$, we have the following representations for the electric fields.

$$\left.\begin{aligned} E_{xe} &= [ik_{\perp}J_n^{'}(k_{\perp}\rho)\cos\varphi + \frac{n}{\rho}J_n(k_{\perp}\rho)\sin\varphi]\times \\ &\quad P_e k_z \exp(in\varphi)\exp[i(k_z z-\omega t)] \\ E_{ye} &= [ik_{\perp}J_n^{'}(k_{\perp}\rho)\sin\varphi - \frac{n}{\rho}J_n(k_{\perp}\rho)\cos\varphi]\times \\ &\quad P_e k_z \exp(in\varphi)\exp[i(k_z z-\omega t)] \\ E_{ze} &= P_e k_{\perp}^2 J_n(k_{\perp}\rho)\exp(in\varphi)\exp[i(k_z z-\omega t)] \end{aligned}\right\} \quad (12a)$$

$$\left.\begin{aligned} E_{xm} &= -[\frac{n}{\rho}J_n(k_{\perp}\rho)\cos\varphi - ik_{\perp}J_n^{'}(k_{\perp}\rho)\sin\varphi]\times \\ &\quad P_m \omega\mu \exp(in\varphi)\exp[i(k_z z-\omega t)] \\ E_{ym} &= -[\frac{n}{\rho}J_n(k_{\perp}\rho)\sin\varphi + ik_{\perp}J_n^{'}(k_{\perp}\rho)\cos\varphi]\times \\ &\quad P_m \omega\mu \exp(in\varphi)\exp[i(k_z z-\omega t)] \\ E_{zm} &= 0 \end{aligned}\right\} \quad (12b)$$

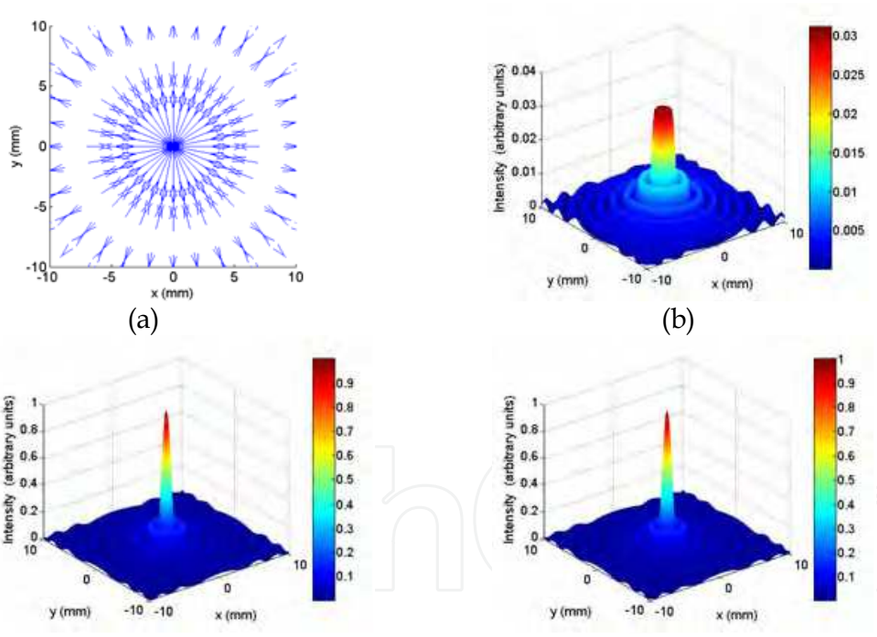

(a) (b) (c) (d)

Fig. 3. TM_0 mode Bessel beam. (a) Instant vector diagram for the transverse component of the electric field ($t=0$, $z=0$). (b) The transverse electric field intensity ($I_{\perp}=|E_{\rho e}|^2+|E_{\varphi e}|^2$). (c) The longitudinal electric field intensity ($I_z=|E_{ze}|^2$) and (d) the total electric filed intensity ($I=I_{\perp}+I_z$). The color bars illustrate the relative intensity. The relevant parameters are $\lambda=3mm$, $k_{\perp}=2.004mm^{-1}$, $k_z=0.608mm^{-1}$, and $R=10mm$.

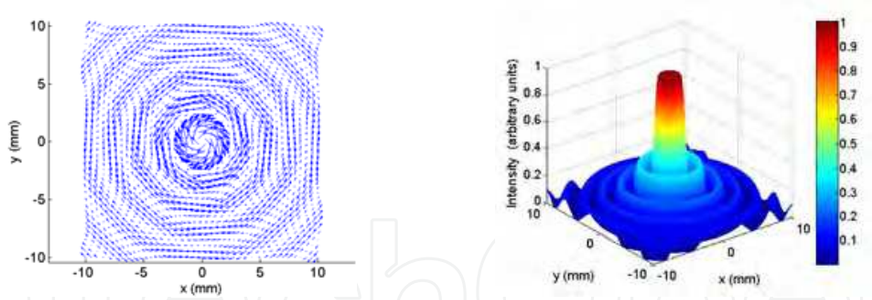

(a) (b)

Fig. 4. TE_0 mode Bessel beam. (a) Instant vector diagram for the transverse component of the electric field ($t = 0$, $z = 0$). (b) The transverse electric field intensity. The relevant parameters are the same as in Fig. 3, except $k_\perp = 1.503 mm^{-1}$, and $k_z = 1.459 mm^{-1}$.

The total electric fields of E_x and E_y are given by, respectively

$$E_x = A_1 E_{xe} + A_2 E_{xm}, \qquad E_y = A_1 E_{ye} + A_2 E_{ym} \tag{13}$$

where A_1 and A_2 are the proportional coefficients. Let $P_e = 1$, then $P_m = i\sqrt{\varepsilon/\mu}$. Substituting (12) into (13), we can deduce the following representations:

$$E_x = E_{xA}\exp(i\theta_1)\exp(in\varphi)\exp[i(k_z z - \omega t)], \qquad E_y = E_{yA}\exp(i\theta_2)\exp(in\varphi)\exp[i(k_z z - \omega t)] \tag{14}$$

where

$$E_{xA} = \sqrt{(B_1\sin\varphi)^2 + (B_2\cos\varphi)^2}, \qquad E_{yA} = \sqrt{(B_1\cos\varphi)^2 + (B_2\sin\varphi)^2},$$

$$B_1 = \frac{A_1 n k_z}{\rho} J_n(k_\perp\rho) - A_2 k k_\perp J_n'(k_\perp\rho), \qquad B_2 = A_1 k_\perp k_z J_n'(k_\perp\rho) - A_2\frac{nk}{\rho} J_n(k_\perp\rho),$$

$$\theta_1 = \arctan(\frac{B_2\cos\varphi}{B_1\sin\varphi}), \qquad \theta_2 = \arctan(-\frac{B_2\sin\varphi}{B_1\cos\varphi}).$$

The polarization states of Bessel beams are discussed as follows:

Case 1) $\theta_2 - \theta_1 = K\pi$, where $K = 0,1,2...$ is an integer. The Bessel beam is linearly polarized. To satisfy this case and assume that $n = 0$, it is demanded from (14) that $A_1 = 0$ and $A_2 \neq 0$, or $A_1 \neq 0$ and $A_2 = 0$. Under these conditions, we can acquire the zero-order Bessel beam with linear polarization, as shown schematically in Figs. 5 and 6.

Case 2) $\theta_2 - \theta_1 = +\pi/2$ and $E_{xA} = E_{yA}$. The Bessel beam is left-hand circularly polarized. To satisfy these requirements, the demand of $A_1/A_2 = +k/k_z$ can be derived from (14). The left-hand circularly polarized Bessel beam is illustrated in Fig. 7.

Case 3) $\theta_2 - \theta_1 = -\pi/2$ and $E_{xA} = E_{yA}$. The Bessel beam become right-hand circularly polarized. Similarly, the demand of $A_1/A_2 = -k/k_z$ is needed. Fig. 8 shows the right-hand circularly polarized Bessel beam.

Case 4) In other cases, the Bessel beam is elliptically polarized.

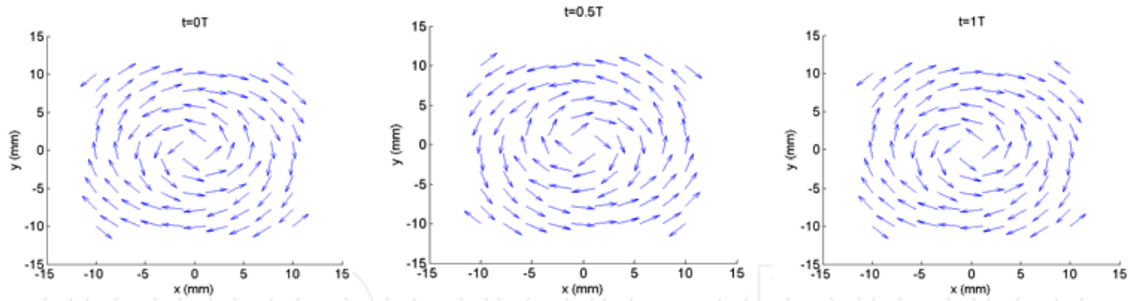

(a) (b) (c)

Fig. 5. Linearly polarized Bessel beam. (a)-(c) Vector diagrams of the transverse component of the electric field at three different instants: $t = 0$, $t = 0.5T$, $t = T$, $T = 2\pi/\omega$, respectively. The parameters used in Fig. 5 are $k_\perp/k = 0.25$, $n = 0$, $A_1 = 0$, and $A_2 \neq 0$.

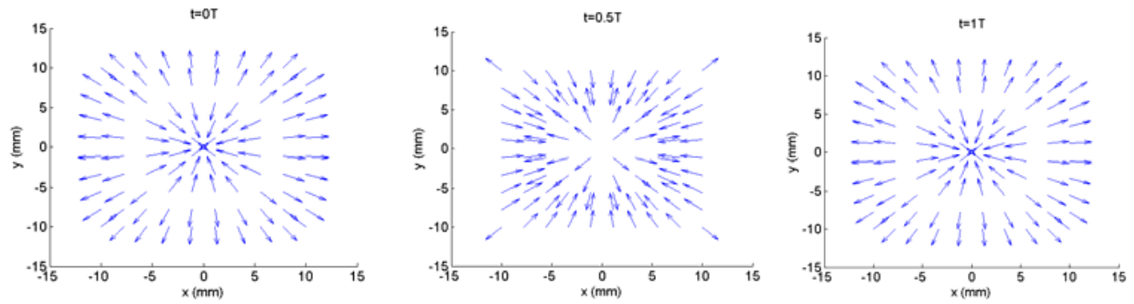

(a) (b) (c)

Fig. 6. Linearly polarized Bessel beam. (a)-(c) Vector diagrams of the transverse component of the electric field at three different instants: $t = 0$, $t = 0.5T$, $t = T$, respectively. The parameters used in Fig. 6 are the same as in Fig. 5, except $A_1 \neq 0$, and $A_2 = 0$.

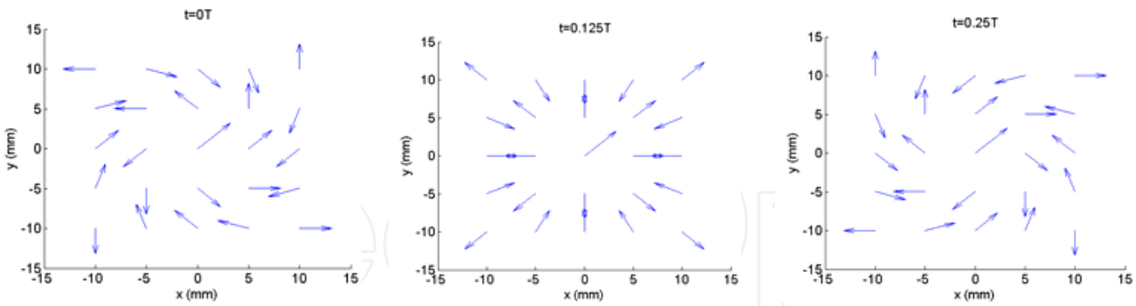

(a) (b) (c)

Fig. 7. Left-hand circularly polarized Bessel beam. (a)-(c) Vector diagrams of the transverse component of the electric field at three different instants: $t = 0$, $t = 0.125T$, $t = 0.25T$, respectively. The relevant parameters are $k_\perp/k = 0.4$, and $A_1/A_2 = +k/k_z$.

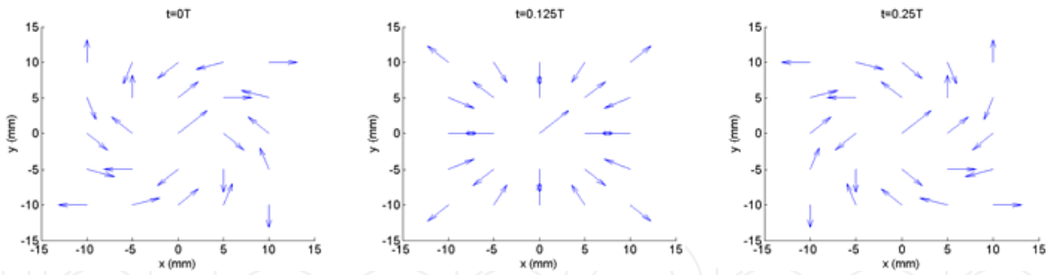

(a) (b) (c)

Fig. 8. Right-hand circularly polarized Bessel beam. (a)-(c) Vector diagrams of the transverse component of the electric field at three different instants: $t = 0$, $t = 0.125T$, $t = 0.25T$, respectively. The relevant parameters are $k_\perp / k = 0.4$, and $A_1 / A_2 = -k / k_z$.

2.2.3 Energy Density and Poynting Vector

Using the above equations (11), the total time-average electromagnetic energy density for the transverse modes, TE or TM, is calculated to be

$$\overline{w} = \frac{1}{4}\varepsilon |\vec{E}|^2 + \frac{1}{4}\mu |\vec{H}|^2 = \frac{1}{4}\varepsilon\{(k_\perp J_n)^2 + (k^2 + k_z^2)[(\frac{nJ_n}{\rho})^2 + (k_\perp J_n^{'})^2]\} \tag{15}$$

And the time-average Poynting vector power density is given by

$$\overline{\vec{S}} = \frac{1}{2}\mathrm{Re}(\vec{E} \times \overline{\vec{H}}^{*}) = \omega\varepsilon k_z[(\frac{nJ_n}{\rho})^2 + (k_\perp J_n^{'})^2]\vec{z} + \frac{n\omega\varepsilon}{\rho}(k_\perp J_n)^2\vec{\varphi} \tag{16}$$

From (15) or (16), it can immediately be seen that neither $\overline{w}$ nor $\overline{\vec{S}}$ depends on the propagation distance z . This means the time-average energy density does not change along the z axis, and our solutions clearly represent nondiffracting Bessel beams. In addition, from (16), we note that $\overline{\vec{S}}$ has the longitudinal and transverse components, which determine the flow of energy along the z axis and perpendicular to the z-axis, respectively. However, when n=0, corresponding to TM_0 or TE_0 mode, $\overline{\vec{S}}$ is directed strictly along the z-axis and is proportional to J_1^2 .

3. Generation of pseudo-Bessel Beams by BOEs (Yu & Dou, 2008c; Yu & Dou, 2008d)

In optics, lots of methods for creating pseudo-Bessel Beams have been suggensted, such as narrow annular slit (Durnin et al., 1987), computer-generated holograms (CGHs) (Turunen et al., 1988), Fabry-Perot cavity (Cox & Dibble, 1992), axicon (Scott & McArdle, 1992), optical refracting systems (Thewes et al., 1991), diffractive phase elements (DPEs) (Cong et al., 1998) and so on. However, at millimeter and sub-millimeter wavebands, only two methods of production Bessel beams have been proposed currently, i.e., axicon (Monk et al., 1999) and computer-generated amplitude holograms (Salo et al., 2001; Meltaus et al., 2003). Although the method of using axicon is very simple, only a zero-order Bessel beam can be generated. The other method relying on holograms can produce various types of diffraction-free beams, but their diffraction efficiencies are only around 45% (Arlt & Dholakia, 2000) owing to using amplitude holograms. In order to overcome these limitations mentioned above, in our work,

binary optical elements (BOEs) are employed and designed for producing pseudo-Bessel Beams in millimeter and sub-millimeter range for the first time. The suitable design tool is to combine a genetic algorithm (GA) for global optimization with a two-dimensional finite-difference time-domain (2-D FDTD) method for rigours eletromagnetic computation.

3.1 Description of the design tool

3.1.1 FDTD method computational model

The electric field distribution of the *nth* -order Bessel beam in the cylindrical coordinates system is rewritten as：

$$E(\rho,\varphi,z) = E_0 J_n(k_\perp \rho)\exp(in\varphi)\exp(ik_z z) \tag{17}$$

All Bessel beams are circularly symmetric, thus our calculations are concerned only with radically symmetric system. The feature sizes of BOEs are on the order of or less than a millimeter wavelength, the methods of full wave analysis are needed to calculate the diffractive fields of BOEs. The 2-D FDTD method (Yee, 1966) is employed to compute the field diffracted by the BOE in our work. The Computational model of the FDTD method is shown schematically in Fig. 9, in which the BOE is used to convert an incident Gaussian-profile beam on the input plane into a Bessel-profile beam on the output plane. z_1 is the distance between the input plane and the BOE, and z_2 is the distance between the BOE and the output plane; the aperture radius of the BOE, which is represented by R , is the same as that of the input and output planes; n_1 and n_2 represent the refractive indices of the free space and the BOE, respectively; and z is the symmetric axis and the magnetic wall is set on it to save the required memory and computing time.

When a Gaussian beam is normally incident from the input plane onto the left side of the BOE, its wave front is modulated by the BOE, and a desired Bessel beam is obtained on the output plane. It is worthy to point out that our design goal is to acquire a desired Bessel beam in the near field (i.e. the output plane). If one wants to obtain a desired field in the far field, an additional method, like angular-spectrum propagation method (Feng et al.,2003), should be employed to determine the far field.

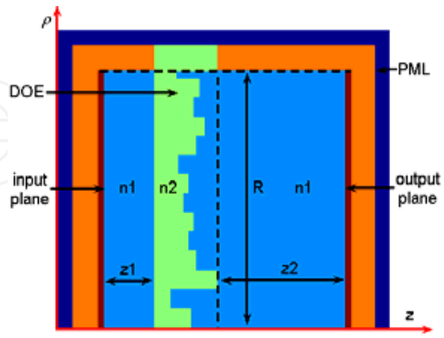

Fig. 9. Schematic diagram of 2-D FDTD computational model

3.1.2 Genetic Algorithm (GA)

To fabricate conveniently in technics, the DOE, with circular symmetry and aperture radius R , should be divided into concentric rings with identical width δ but different

depth x , as shown in Fig. 10. The width δ equals R/K , K is a prescribed positive integer. The maximal depth of a ring is $x_{\max} = \lambda/(n_2 - 1)$, in which n_2 is the refractive index of the BOE. In BOEs design, the depth x of each ring can take only a discrete value. Provided that the maximal depth of a ring is quantified into M -level, in general case, $M = 2^a$, where a is a integer, the minimal depth of a ring is $\Delta x = x_{\max}/M$. Therefore, the depth x of each ring can take only one of the values in the set of $\{\Delta x, 2\Delta x, ..., M\Delta x\}$. Thus, the different combination of the depth x of each ring, i.e., $X = \bigcup_{k=1}^{K} \{x_k\}$, where $x_k \in \{\Delta x, 2\Delta x, ..., M\Delta x\}$, represents the different BOE profile. To obtain the BOE profile which satisfies the design requirement , the different combination X should be calculated, and the optimum combination is gained finally. In fact, this is a combinatorial optimization problem (COP). The GA (Haupt, 1995; Weile & Michielssen, 1997) is adopted for optimizing the BOE profile. It operates on the chromosome, each of which is composed of genes associated with a parameter to be optimized. For instance, in our case, a chromosome corresponds to a set X which describes the BOE profile, and a gene corresponds to the depth x of a ring.

The first step of the GA is to generate an initial population, whose chromosomes are made by random selection of discrete values for the genes. Next, a fitness function, which describes the different between the desired field E^d and the calculated field E^c obtained by using 2-D FDTD method, will be evaluated for each chromosome. In our study, the fitness function is simply defined as:

$$fitness = \sum_{u=1}^{U} (|E_u^c| - |E_u^d|)^2 \tag{18}$$

in which E_u^c and E_u^d are the calculated field and the desired field at the uth sample ring of the output plane, respectively. Then, based on the fitness of each chromosome, the next generation is created by the reproduction process involved crossover, mutation, and selection. Last, the GA process is terminated after a prespecified number of generations $Gen_{\max}$. The flow chart of the GA procedure is shown in Fig. 11.

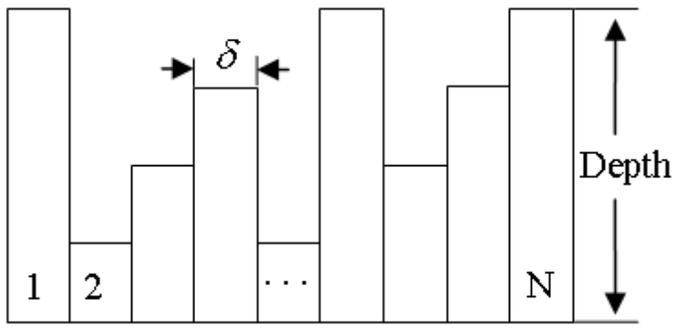

Fig. 10. Division of the BOE profile into the rings with identical width δ but different depths x

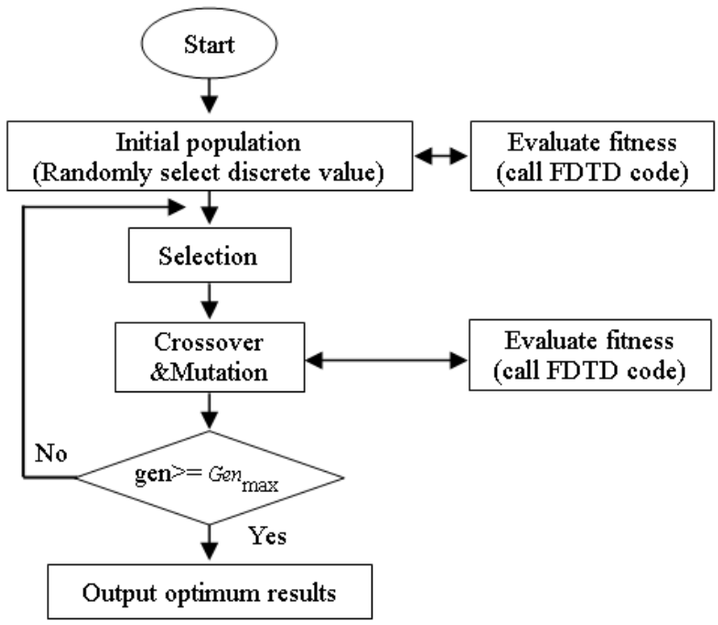

Fig. 11. The flow chart of the GA procedure

3.2 Numerical simulation results

In order to evaluate the quality of the designed BOE, we introduce the efficiency η and the root mean square (RMS) describing the BOE profile error (Feng et al.,2003), which are defined as, respectively.

$$\eta = \frac{\sum_{u=1}^{U} |E_u^c|^2 S_u^c}{\sum_{v=1}^{V} |E_v^i|^2 S_v^i} \tag{19}$$

$$RMS = \left[\frac{1}{U-1} \sum_{u=1}^{U} (|E_u^c|^2 - |E_u^d|^2)^2 \right]^{1/2} \tag{20}$$

where S_v^i and S_u^c are the areas of the *vth* and *uth* sample ring of the input and output planes, respectively; E_v^i is the incident field at the *vth* sample ring of the input plane, and E_u^c and E_u^d are the calculated field and the desired field at the *uth* sample ring of the output plane. To demonstrate the utility of the design method, we present three examples herein in which an incident Gaussian beam is converted into a zero-order, a first order and a second order Bessel beam respectively. The same parameters in three examples are as follows: an incident Gaussian beam waist of $w_0 = 4\lambda$ $n_1 = 1.0$, $n_2 = 1.45$, $z_1 = 2\lambda$, $z_2 = 6\lambda$, $\delta = \lambda/18$, $R = 8\lambda$, $K = 144$, $M = 8$, $U = V = K$. From three cases, it is clearly seen that the fields diffracted by the designed BOE's on the output plane agree well with the desired electric field intensity distributions.

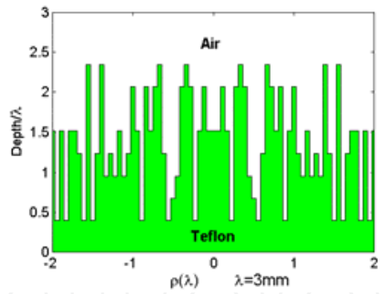

(a)

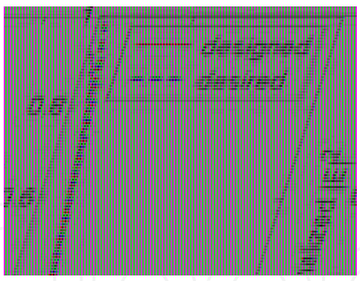

(b)

(c)

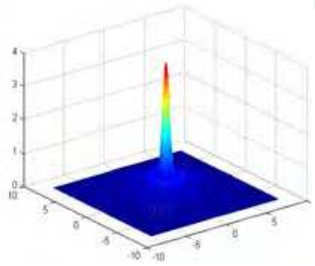

(d)

Fig. 12. Generation of a J_0 beam on the output plane. $\lambda = 3mm$, $k_{\perp} = 0.7635mm^{-1}$, $\eta = 94.494\%$ and $RMS = 5.562\%$. (a) Part of the optimized BOE profile. (b) The desired and the designed transverse intensity distribution on the output plane. (c) The 2-D transverse intensity distribution plotted in a gray-level representation, and (d) the 3-D transverse intensity distribution.

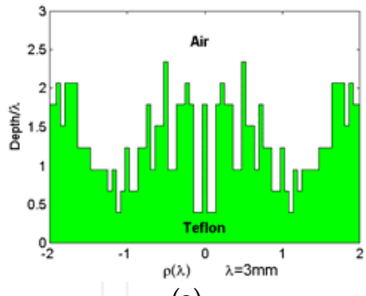

(a)

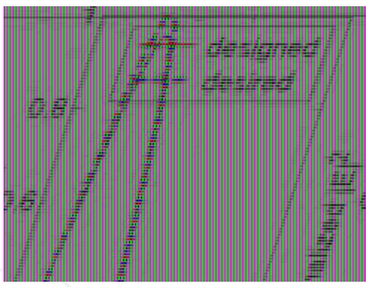

(b)

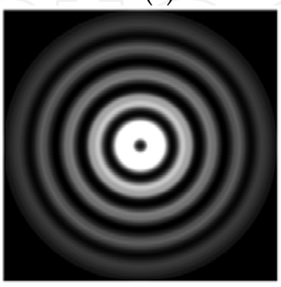

(c)

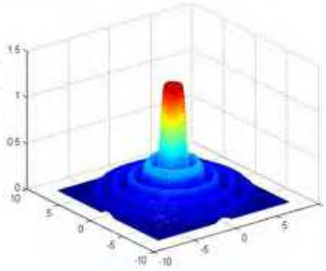

(d)

Fig. 13. Production of a J_1 beam on the output plane. $\lambda = 3mm$, $k_{\perp} = 0.6911mm^{-1}$, $\eta = 96.283\%$ and $RMS = 2.806\%$. (a) Part of the optimized BOE profile. (b) The desired and the designed transverse intensity distribution on the output plane. (c) The 2-D transverse intensity distribution, and (d) the 3-D transverse intensity distribution.

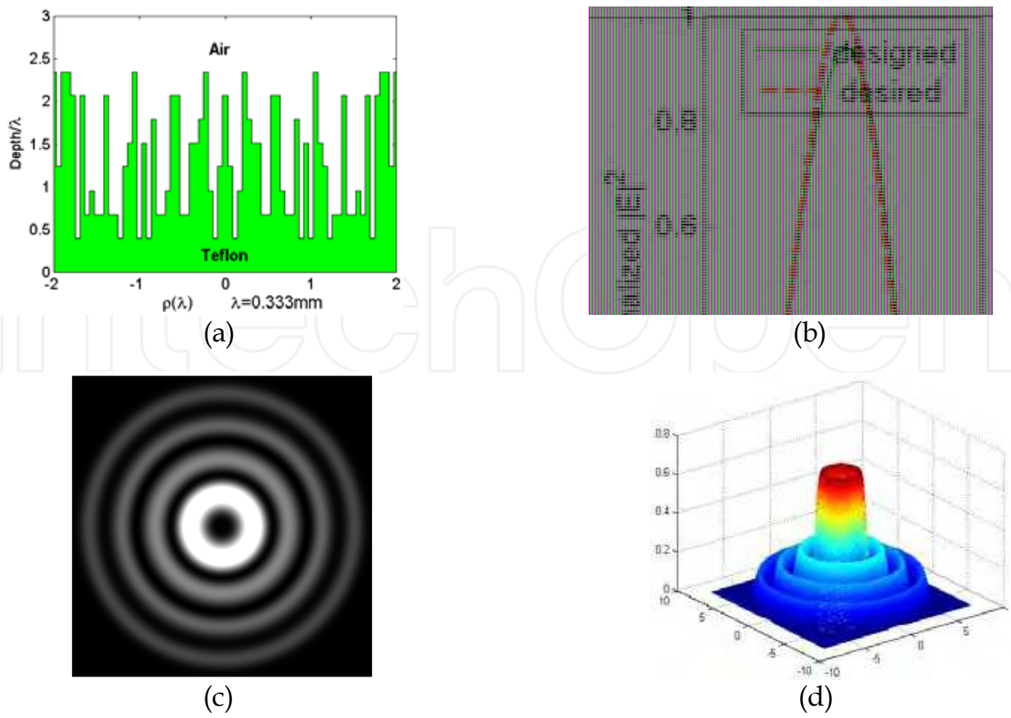

Fig. 14. Creation of a J_2 Bessel beam on the output plane. $\lambda = 0.333mm$, $k_{\perp} = 5.6406mm^{-1}$, $\eta = 97.263\%$ and $RMS = 1.845\%$. (a) Part of the optimized BOE profile. (b) The desired and the designed transverse intensity distribution on the output plane. (c) The 2-D transverse intensity distribution, and (d) the 3-D transverse intensity distribution.

4. Production of approximate Bessel beams using binary axicons (Yu & Dou, 2009)

Currently, numerous ways for generating pseudo-Bessel beams have been proposed, among which using axicon is the most popular method, owing to its simplicity of configuration and easy realization. However, at millemter and sub-millimter wavebands, classical cone axicons are usually bulk ones and therefore have many disadvantages, like heavy weight, large volume and thus increased absorption loss in the material. These limitations together make them extremely difficult in miniaturizing and integrating in millemter and sub-millimter quasi-optical systems. To overcome these problems, binary axicons, based on binary optical ideas, are introduced in our study and designed for producing pseudo-Bessel beams at sub-millimter wavelengths. The designed binary axicons are more convenient to fabricate than holographic axicons (Meltaus et al., 2003; Courtial et al., 2006) and, become thinner and less lossy in the material than classical cone axicons (Monk et al., 1999; Trappe et al., 2005; Arlt & Dholakia, 2000). In order to analyze binary axicons accurately when illuminated by a plan wave in sub-millimter range, the rigorous electromagnetic analysis method, that is, a 2-D FDTD method for determining electromagnetic fields in the near region in conjunction with Stratton-Chu formulas for obtaining electromagnetic fields in the far region, is adopted in our work. Using this combinatorial method, the properties of approximate Bessel beams generated by the designed binary axicons are analyzed.

4.1 Binary axicon design

A classical cone axicon, introduced firstly by McLeod in 1954 (McLeod, 1954), is usually a bulk one, as illustrated in Fig. 15(a), in which D is the aperture diameter and γ is the prism angle. Based on binary optical ideas, the profile of a binary axicon, whose performance required is equivalent to that of a bulk one, can be easily formed. Assuming straight-ray propagation through the bulk axicon, the relation between the phase retardation $\varphi(\rho)$ and the surface height $h(\rho)$ is given as (Feng et al., 2003)

$$h(\rho) = \varphi(\rho)/[(n_2 - n_1)k] \tag{21}$$

where k is the free space wave number, n_1 and n_2 are the refractive indexes of the air and the axicon, respectively. To generate the continuous profile of the binary axicon, the equivalent transformation can be used by (Hirayama et al., 1996)

$$h(\rho) = [\varphi(\rho) \bmod 2\pi]/[(n_2 - n_1)k] \tag{22}$$

The continuous profile of the binary axicon produced by (22) is shown in Fig. 15(c). For the multilevel axicon, the profile is quantized into equal height step Δ . The quantized height is given by

$$h_q(\rho) = \text{int}[h(\rho)/\Delta]\Delta \tag{23}$$

where $\Delta = h_{\max}/M$, $h_{\max} = \lambda/(n_2 - n_1)$ and M is the number of levels. Eq. (23) generates the multilevel profiles of the binary axicon. The schematic diagram of the 4-level binary axicon is illustrated in Fig. 15 (d). It is known that the larger the number of levels is, the higher the diffraction efficiency is, however, the higher the difficulty of manufacture becomes. Therefore, the compromise between the diffraction efficiency and the difficulty of manufacture should be considered when determining the number of levels. In our work the selection of the 32-level binary axicon is made. From Figs. 15(c) and 15(d), we can see easily that the designed binary axicon is not only more compact than the classical cone axicon, but also simpler to fabricate than the holographic axicon.

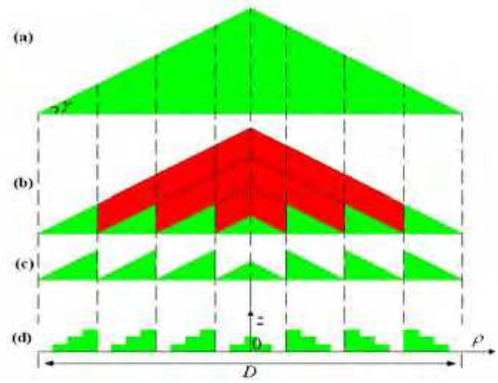

Fig. 15. The design process of a binary axicon. (a) A bulk axicon. (b) An axicon removed the unwanted material (red part). (c) An equivalent binary axicon with continuous profile. (d) An equivalent binary axicon quantized into four levels.

4.2 Rigorous electromagnetic analysis method

Because of rotational symmetry of the binary axicon, a 2-D FDTD method is applied to evaluate the electromagnetic fields diffracted by the binary axicon in the near region. The computational model of the 2-D FDTD method is shown schematically in Fig. 16, in which

the binary axicon is utilized to convert an incident beam into a pseudo-Bessel beam. To stimulate the entire 2-D FDTD grid, a total-scattered field approach is applied to introduce a normally incident plane wave. In this approach the connecting boundary serves to connect the total and the scattered field regions, and is the location at which the incident field is introduced. Because of the limitation of computational time and memory, the computational range of the 2-D FDTD method is truncated by using perfectly matched layer (PML) absorbing boundary conditions (ABCs) in the near region. Therefore, in order to accurately determine the electromagnetic fields in the far region, Stratton-Chu integral formulas are applied and given by (Stratton, 1941)

$$\begin{aligned}\vec{E}(\vec{r}) &= \int_L \left\{-i\omega\mu\left[\vec{n}\times\vec{H}(\vec{r}')\right]G_0(\vec{r},\vec{r}') + \left[\vec{n}\times\vec{E}(\vec{r}')\right]\times\nabla' G_0(\vec{r},\vec{r}') + \left[\vec{n}\bullet\vec{E}(\vec{r}')\right]\nabla' G_0(\vec{r},\vec{r}')\right\} dL' \\ \vec{H}(\vec{r}) &= \int_L \left\{i\omega\varepsilon\left[\vec{n}\times\vec{E}(\vec{r}')\right]G_0(\vec{r},\vec{r}') + \left[\vec{n}\times\vec{H}(\vec{r}')\right]\times\nabla' G_0(\vec{r},\vec{r}') + \left[\vec{n}\bullet\vec{H}(\vec{r}')\right]\nabla' G_0(\vec{r},\vec{r}')\right\} dL'\end{aligned} \tag{24}$$

where $\vec{r} = (\rho, z)$ and $\vec{r}\,' = (\rho', z')$ denote an arbitrary observation point in the far region and an source point on the output boundary of the 2-D FDTD model, respectively; unit vector $\vec{n}$ is the outer normal of the closed curve, L, of the output boundary; $G_0(\vec{r},\vec{r}') = -iH_0^{(2)}(k|\vec{r}-\vec{r}'|)/4$, is the 2-D scalar Green's function in free space, $H_0^{(2)}$ is the zero-order Hankel function of the second kind and k is the wave number in free space; ω is the angular frequency; ε and μ are the permittivity and permeability, respectively.

In short, our electromagnetic analysis method is to join the 2-D FDTD method for computing the fields diffracted by the binary axicon in the near region with the Stratton-Chu integral formulas for obtaining its diffractive fields in the far region. It can be implemented by the following procedure: First, we carry out the 2-D FDTD computation and obtain the near fields, $\vec{E}(\vec{r}')$ and $\vec{H}(\vec{r}')$, on the output boundary. Then, these fields can be regarded as secondary sources and substituted into (24) to calculate the fields, $\vec{E}(\vec{r})$ and $\vec{H}(\vec{r})$, at arbitrary observation point in the far region. Note that the integral herein is over the closed curve, L, of the output boundary.

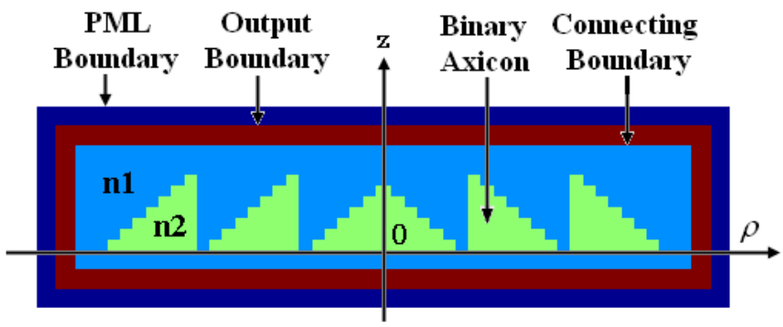

Fig. 16. Schematic diagram of 2-D FDTD computational model, where the 8-level binary axicon is embedded into FDTD grid.

4.3 Demonstration of equivalence

To demonstrate the equivalent performance between the bulk axicon and the designed binary axicon, Fig. 17 shows the on-axis intensity distributions for both the bulk axicon and the 32-level binary axicon. In this case both axicons, with the same aperture

diameter $D = 40\lambda$ and prism angle $\gamma = 10^0$, are normally illuminated by a plane wave of unit amplitude. Other parameters used in Fig. 17 are as follows: an incident wavelength is $\lambda = 0.32mm$ ($f = 0.94\text{THz}$), the refractive indexes of the axicon and the air are $n_2 = 1.4491$ (Teflon) and $n_1 = 1.0$, respectively. Two distributions exhibit some differences in the near region ($z < 75\lambda$). The reason is that the binary axicon suffers more from edge diffraction and truncation effects (Trappe et al., 2005). The effects can also be seen from Fig. 18(b), which has more burr than Fig. 18(a) in the near region. However, two curves show a good agreement in the region ($z > 75\lambda$), where the propagating beam can be best approximated by the Bessel beam in terms of its intensity profile. Thus, the performance of the designed binary axicon is equivalent to that of the bulk one. In order to further demonstrate the equivalent effect between two axicons, we extend our 2-D FDTD calculated region to 200λ along z-axis, and display their electric-field amplitudes in a pseudo-color representation in Fig. 18. It can also be seen that the designed binary axicon has the same performance as the bulk one.

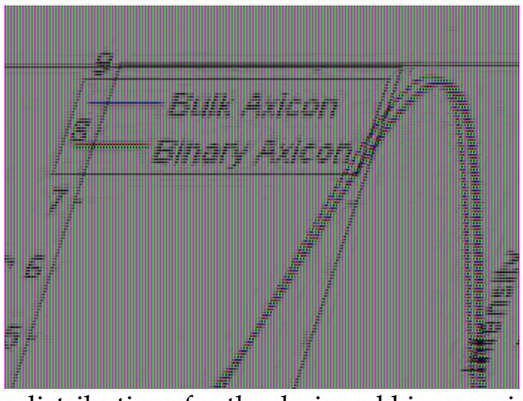

Fig. 17. The axial intensity distributions for the designed binary axicon and the bulk one.

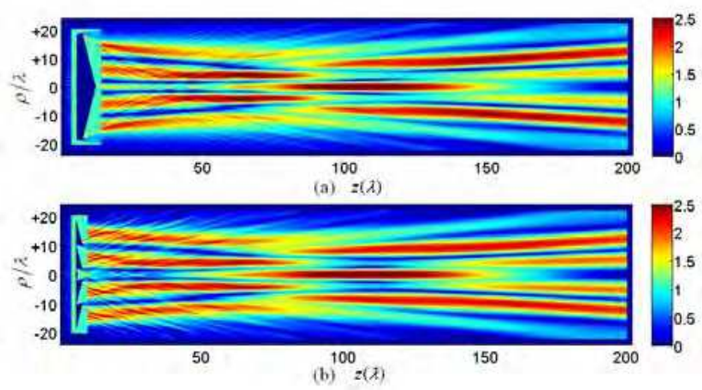

Fig. 18. Electric-field amplitude patterns plotted in a pseudo-color representation. (a) For the bulk axicon. (b) For our designed binary axicon.

4.4 Properties of pseudo-Bessel beam

In order to study the properties of a pseudo-Bessel beam, the other 32-level binary axicon having aperture diameter $D = 44\lambda$ and prism angle $\gamma = 12^0$, are examined. Other parameters used in this example are the same as in Fig .17. When this axicon is normally illuminated by a plane wave of unit amplitude, its axial and transverse intensity distributions at three

representative values of z : $z = 0.8Z_{\max}$, $Z_{\max}$ and $1.2Z_{\max}$ are shown in Figs. 19(a)-19(d), respectively. It can be seen clearly from Fig. 19(a) that the on-axis intensity increases with oscillating, and reaches its maximum axial intensity then decreases quickly, as the propagation distance z increases. The maximum value of on-axis intensity in Fig. 19(a) is 10.297 , located at $Z_{\max} = 125.4\lambda$. As shown in Fig. 19(a), if $L_{\max}$ is defined as the maximum propagation distance of a pseudo-Bessel beam, we can obtain $L_{\max} \approx 230\lambda$. In addition, according to geometrical optics (Trappe et al., 2005), a limited diffraction range $L = 227\lambda$ is estimated by: L= D/(2 tan β) and $\sin(\beta + \gamma) = n_1 \sin\gamma$. We discover two results almost coincide. From Figs. 19(b)-19(d) we can observe that their transverse intensity distributions are approximations to Bessel function of the first kind. The radii of their central spot are only about 3.5λ . This indicates that the transverse intensity distribution of pseudo-Bessel beam is highly localized. It is also interesting to point out that the radius size of 3.5λ is very close to the value of 3.4λ , which is determined roughly from the first zero of the Bessel function ($2.4048\lambda/(2\pi \sin\beta)$) (Trappe et al., 2005).

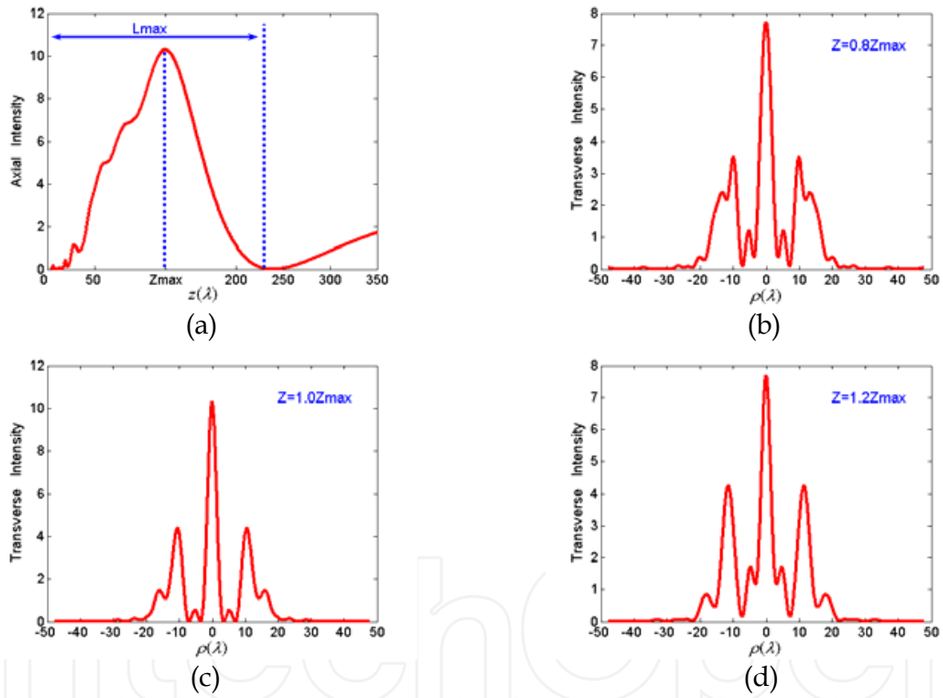

Fig. 19. The axial and transverse intensity distributions for the designed binary axicon. (a) The on-axis intensity versus propagation distance z . (b) The transverse intensity distribution at $z = 0.8Z_{\max}$ plane. (c) $z = 1.0Z_{\max}$. (d) $z = 1.2Z_{\max}$.

5. Propagation characteristic (Yu & Dou, 2008e)

The most interesting and attractive characteristic of Bessel beam is diffraction-free propagation distance. In optics, the comparisons of maximum propagation distance had been done between apertured Bessel and Gaussian beams by Durnin (Durnin, 1987; Durnin et al., 1988) and Sprangle (Sprangle & Hafizi, 1991), respectively. However, the completely

contrary conclusions were derived by them, owing to the difference between their contrast criteria. Because Bessel beams have many potential applications at millimeter and sub-millimeter wavebands, therefore, it is necessary and significant that the comparison is carried out at these bands. A new comparison criterion in the spectrum of millimeter and sub-millimeter range has been proposed by us. Under this criterion, the numerical results obtained by using Stratton-Chu formulas instead of Fresnel-Kirchhoff diffraction integral formula are presented; and a new conclusion is drawn.

5.1 Reviews of comparisons of Durnin and Sprangle

In this Subsection, the comparisons done by Durnin and Sprangle respectively are reviewed at first. Because of the circular symmetries of Bessel and Gaussian beams, thus our calculations are concerned only with circularly symmetric system. Let $(\rho',0)$ and (ρ,z) be the coordinates of a pair of points on the incident and receive planes, respectively. In optics, it is well known that scalar diffraction theory yields excellent results when the wavelength is small compared with the size of the aperture and the propagation angles are not too steep (Durnin, 1987). In the Fresnel approximation the amplitude $A(\rho,z)$ at a distance z can be obtained from Fresnel-Kirchhoff diffraction integral formula (Jiang et al., 1995)

$$A(\rho,z)=\exp(ikz+\frac{ik\rho^2}{2z})(\frac{k}{iz})\times\int_0^R A(\rho',0)J_0(\frac{k\rho'\rho}{z})\exp(\frac{ik\rho'^2}{2z})\rho'\mathrm{d}\rho' \tag{25}$$

where $\rho=\sqrt{x^2+y^2}$, $\rho'=\sqrt{x'^2+y'^2}$, R is the aperture radius of incident plane, and

$$A(\rho',0)=\begin{cases}J_0(k_\perp\rho') & \text{Bessel beam}\\ \exp(-\rho'^2/w_0^2) & \text{Gaussian beam}\end{cases} \tag{26}$$

for all $\rho'<R$, and zero for all $\rho'>R$, where $k_\perp$ is the radial wave number and w_0 is the waist radius of Gaussian beam. When $\rho=0$ in (25), the axial intensity distribution $I_A(0,z)$ can be given by

$$I_A(0,z)=\left|A(0,z)\right|^2=\left(\frac{k}{z}\right)^2\times\left|\int_0^R A(\rho',0)\exp(\frac{ik\rho'^2}{2z})\rho'\mathrm{d}\rho'\right|^2 \tag{27}$$

According to Durnin's comparison criterion (Durnin, 1987; Durnin et al., 1988) : $\rho_0=w_0$, that is, on the incident plane ($z'=0$), the central spot radius ρ_0 of zero-order Bessel beam (i.e. J_0 beam) is equal to the waist radius w_0 of Gaussian beam, as displayed in Fig. 20(a), where $\rho_0=w_0=100um$, $k_\perp=2.405/\rho_0$, $R=2mm$, $\lambda=0.6328um$, we calculate the $I_A(0,z)$ versus z curves by using (27), which are shown in Fig. 20(b). It can be seen clearly from Fig. 20(b) that the Bessel beam propagates farther than the Gaussian beam.

However, according to Sprangle's comparison criterion (Sprangle & Hafizi, 1991): $w_0=R$, and a J_0 beam has at least one side-lobe on the incident plane, as illustrated in Fig. 21(a), we can obtain the results given in Fig. 21(b). The converse conclusion that the Bessel beam propagates no farther than the Gaussian beam can be easily drawn from Fig. 21(b).

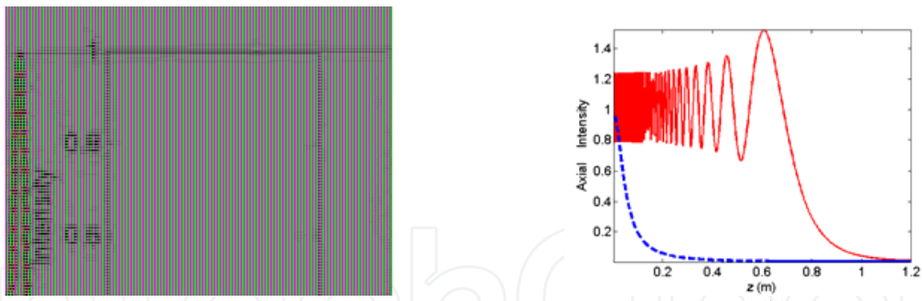

(a) (b)

Fig. 20. The comparison of Durnin. (a) Intensity distributions for a J_0 beam (—) and a Gaussian beam (----) on the incident plane where the beams are assumed to be formed. (b) Axial intensities $I_A(0,z)$ versus propagation distance z .

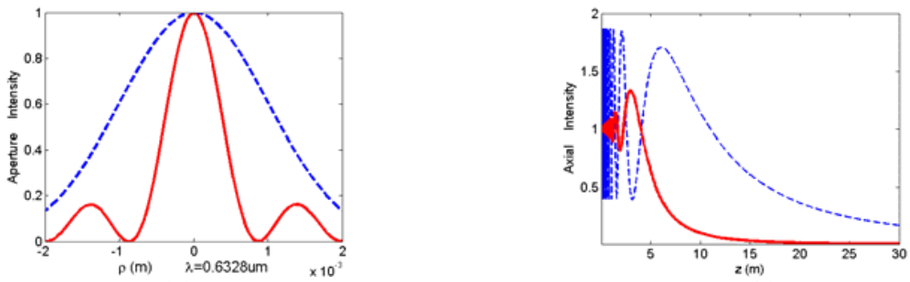

(a) (b)

Fig. 21. The comparison of Sprangle. (a) Intensity distributions for a J_0 beam and a Gaussian beam on the incident plane. (b) Axial intensities $I_A(0,z)$ versus propagation distance z .

The reason why the converse conclusions were obtained by Durnin and Sprangle respectively was that the criteria taken by them were very different. This fact can be seen from Fig. 20(a) and Fig. 21(a). Moreover, the key problem of their criteria is not objective and fair. Under Durnin's criterion, the utilization ration of aperture for the Gaussian beam is very low. In fact, we should not utilize so large aperture to eradiate a Gaussian beam with so small waist radius. However, under Sprangle's criterion, the powers carried by two beams on the incident plane are not equal. Therefore, we propose a new comparison criterion at millimeter wavelengths, which is discussed in the next Subsection.

5.2 Our comparison criterion and results

At millimeter wave bands, it is known that Fresnel-Kirchhoff diffraction integral formula based on scalar theory is not suitable for calculating the diffractive field. The Stratton-Chu formulas are one of the most powerful tools for the analysis of electromagnetic radiation problems. So, they can be credibly used to determine the diffractive field, and rewritten as (Stratton, 1941)

$$\begin{aligned}\vec{E}(\vec{r}) &= \int_S \left\{-i\omega\mu\left[\vec{n}\times\vec{H}(\vec{r}')\right]G_0(\vec{r},\vec{r}') + \left[\vec{n}\times\vec{E}(\vec{r}')\right]\times\nabla' G_0(\vec{r},\vec{r}') + \left[\vec{n}\bullet\vec{E}(\vec{r}')\right]\nabla' G_0(\vec{r},\vec{r}')\right\} dS' \\ \vec{H}(\vec{r}) &= \int_S \left\{i\omega\varepsilon\left[\vec{n}\times\vec{E}(\vec{r}')\right]G_0(\vec{r},\vec{r}') + \left[\vec{n}\times\vec{H}(\vec{r}')\right]\times\nabla' G_0(\vec{r},\vec{r}') + \left[\vec{n}\bullet\vec{H}(\vec{r}')\right]\nabla' G_0(\vec{r},\vec{r}')\right\} dS'\end{aligned} \tag{28}$$

where $\vec{r}=(\rho,z)$, $\vec{r}\,'=(\rho',0)$, $G_0(\vec{r},\vec{r}')=e^{-ik|\vec{r}-\vec{r}'|}/(4\pi|\vec{r}-\vec{r}'|)$, is the scalar Green's function. Let us assume that on the incident plane ($z'=0$) we have a J_0 beam and a Gaussian beam, polarized in the x direction and propagating in the z direction. They are expressed in the following forms, respectively.

$$\begin{cases}\vec{E}(\vec{r}\,')=\vec{x}J_0(k_\perp\rho'), & \vec{H}(\vec{r}\,')=\vec{y}\,J_0(k_\perp\rho')/\eta & \text{Bessel beam}\\ \vec{E}(\vec{r}\,')=\vec{x}\exp(-\rho'^2/w_0^2), & \vec{H}(\vec{r}\,')=\vec{y}\exp(-\rho'^2/w_0^2)/\eta & \text{Gaussian beam}\end{cases} \tag{29}$$

where $\eta=\sqrt{\mu/\varepsilon}$. When $\rho=0$ in (28), the axial intensity distribution $I_A(0,z)$ can be obtained by substituting (29) into (28)

$$I_A(0,z)=\left|\vec{E}(\vec{r})\right|^2=\left|\vec{E}(0,z)\right|^2 \tag{30}$$

In addition, at a certain plane $z=z_f$, the transverse intensity distribution $I_T(\rho,z_f)$ can also be calculated by

$$I_T(\rho,z_f)=\left|\vec{E}(\vec{r})\right|^2=\left|\vec{E}(\rho,z_f)\right|^2 \tag{31}$$

Now, we propose our contrast criterion: the same initial total power and central peak intensity on the same initial aperture. In order to compare conveniently, we also defined the propagation distance as the value of z-axis at which the axial intensity falls to $1/2$. Three cases are presented herein, where the same parameters are $\lambda=3mm$ and $R=10\lambda$. In the first example, their intensity distributions for a J_0 beam and a Gaussian beam on the initial aperture are shown in Fig. 22(a). Using (30), we get the axial intensity distributions along z-axis, as illustrated in Fig. 22(b). For the purpose of observing the propagation process, Figs. 22(c)-22(f) display the transverse intensity distributions at $z=10\lambda,20\lambda,30\lambda,40\lambda$, respectively. From this instance, A conclusion can be easily reach that the propagation distance of the J_0 beam is greater than that of the Gaussian beam, under the condition of the same initial total power and central peak intensity on the same initial aperture. In order to further confirm our conclusion, the other two examples are presented in Fig. 23 and Fig. 24. Apparently, a similar conclusion can be drawn from Figs. 23 and 24.

From Figs. 22(b), 23(b) and 24(b), we can also observe that the axial intensity distributions of Bessel beams oscillate more acutely than those of Gaussian beams. This is because the initial field distributions of Bessel beams near the edges of the aperture are much larger than those of Gaussian beams, and as a result, Bessel beam will suffer more diffraction on the sharp edges of the aperture than Gaussian beams.

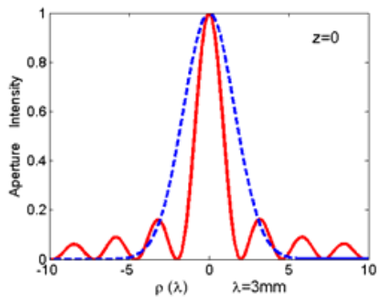

(a)

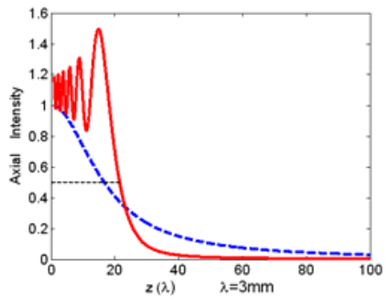

(b)

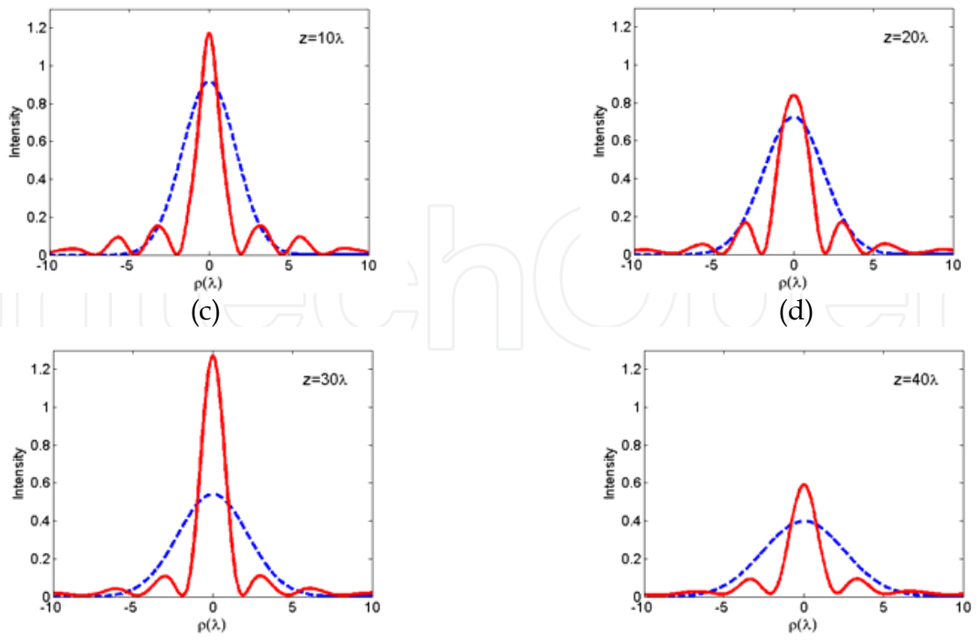

Fig. 22. The first case. (a) Intensity distributions for an apertured Bessel beam (—) and an apertured Gaussian beam (----) on the incident plane. (b) Axial intensities $I_A(0,z)$ versus propagation distance z. (c)-(f) Transverse intensity distributions at $z=10\lambda,20\lambda,30\lambda,40\lambda$, respectively.

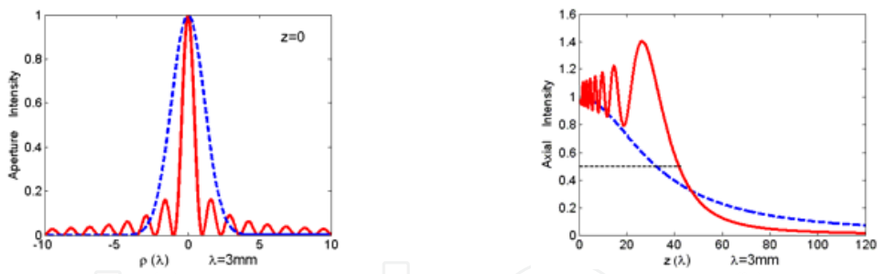

Fig. 23. The second case. (a) Initial Intensity distributions on the incident plane. (b) Axial intensities $I_A(0,z)$ versus propagation distance z.

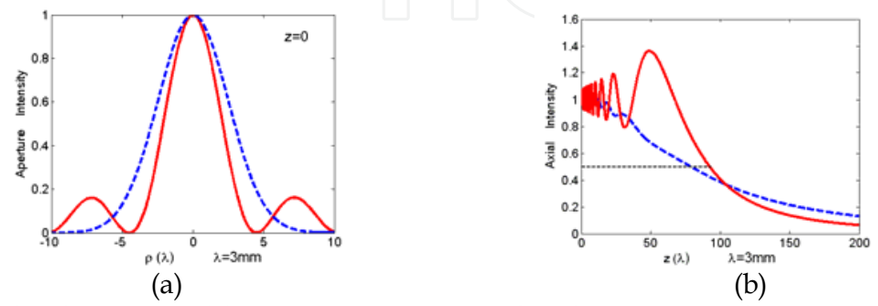

Fig. 24. The last case. (a) Intensity intensity distributions on the apture. (b) Their propagation distance.

6. Applications and Conclusions

The novel properties of the diffraction-free Bessel beams have many significant applications (Bouchal, 2003). In optics, due to the propagation invariance and extremely narrow intensity profile, Bessel beams are applicable in metrology for scanning optical systems. These beams are also suitable for large-scale straightness and measurements (Wang et al., 2003), since they can stand the atmospheric turbulence more than other beams. The imaging applications of the diffraction-free Bessel beams are also presented in (Li & Aruga, 1999), and it has been demonstrated that the imaging produced by Bessel beams can provide a longer focal depth when compared with Gaussian beams. Bessel beams can also be applied to optical interconnection and promotion of free electron laser gain (Li et al., 2006). An increasing attention is devoted to the applications of Bessel beams in nonlinear optics. The third-harmonic generation using Bessel beams was proposed by Tewari and co-workers (Tewari et al., 1996). In addition, Cerenkov second-harmonic generation by nondiffracting Bessel beams in bulk optical crystals was also suggested in (Pandit & Payne, 1997). The application of Bessel beams to increase the Z-scan sensitivity in measurement was demonstrated in (Hughes & Burzler, 1997). The radially polarized Bessel beams were applicable to accelerate the particles of the electron beam (Tidwell et al., 1992). Recently, Bessel beams are used to manipulate micrometer-sized particles. Using the self-reconstruction property of Bessel beam, it is possible to manipulate tiny particles simultaneously in multiple planes (Hegner, 2002; Garces-Chavez et al., 2002). We believe that Bessel beams are prospective for improving the resolution of images in millimeter wave imaging system (Monk, 1999). These beams may also be useful for measurements and power transmission at millimeter and sub-millimeter wavebands.

In optical region of the spectrum, diffraction-free Bessel beams have attracted much interest over the years and have been widely investigated. However, in the millimeter and sub-millimeter wave regions, exploratory work devoted to this field is much less. So, a great deal of contribution should be made to this field in the future.

7. Acknowledgments

This work is supported by NSFC under grant 60621002, the Natural Science Foundation of Fujian Province of China (No.A0610027) and the Key Project of Quanzhou City Science and Technology Program (No.2008G13).

8. References

Arlt, J. & Dholakia, K. (2000). Generation of high-order Bessel beams by use of an axicon. *Opt. Commun.*, Vol. 177, pp. 297-301

Bouchal, Z.; Wagner, J. & Chlup, M. (1998). Self-reconstruction of a distorted nondiffracting beam. *Opt. Commun.*, Vol. 151, No. 4-6, pp. 207–211

Bouchal, Z. (2003). Nondiffracting optical beams: physical properties, experiments, and applications. *Czech. J. phys.*, Vol. 53, No. 7, pp. 537-624

Cox, A. J. & Dibble, D. C. (1992). Nondiffracting beam from a spatially filtered Fabry-Perot resonator. *J. Opt. Soc. Am. A*, Vol. 9, No. 2, pp. 282–286

Cong, W. X.; Chen, N. X. & Gu, B. Y. (1998). Generation of nondiffracting beams by diffractive phase elements. *J. Opt. Soc. Am. A*, Vol. 15, No. 9, pp. 2362–2364

Courtial, J.; Whyte, G.; Bouchal, Z.; et al. (2006). Iterative algorithms for holographic shaping of non-diffracting and self-imaging light beams. *Opt. Express*, Vol. 14, No. 6, pp. 2108–2116

Durnin, J. (1987). Exact solutions for nondiffracting beams. I. The scalar theory. *J. Opt. Soc. Am. A*, Vol. 4, No. 4, pp. 651–654

Durnin, J.; Miceli J. J., Jr. & Eberly, J. H. (1987). Diffraction-free beams. *Phys. Rev. Lett.*, Vol. 58, No. 15, pp. 1499-1501

Feng, D.; Yan, Y. B.; Jin, G. F.; et al. (2003). Rigorous electromagnetic design of finite-aperture diffractive optical elements by use of an iterative optimization algorithm. *J. Opt. Soc. Am. A*, Vol. 20, No. 9, pp. 1739-1745

Garces-Chavez, V.; Mcgloin, D. & Melvill, E. H. (2002). Simultaneous micromanipulation in multiple planes using a self-reconstructing light beam. *Nature*, Vol. 419, No. 6903, pp. 145–147

Haupt, R. L. (1995). An introduction to genetic algorithms for electromagnetics. *IEEE Antennas Propag. Mag.*, Vol. 37, No. 2, pp. 7-15

Hirayama, K.; Glytsis, E. N. & Gaylord, T. K. (1996). Rigorous electromagnetic analysis of diffractive cylindrical lenses. *J. Opt. Soc. Am.* A, Vol. 13, No. 11, pp. 2219–2231

Hughes, S. & Burzler, J. M. (1997). Theory of Z-scan measurements using Gaussian-Bessel beams. *Phys. Rev. A*, Vol. 56, No. 2, pp. R1103–R1106

Hegner, M. (2002). Optics: The light fantastic. *Nature*, Vol. 419, No. 6903, pp. 125–127

Jiang, Z. P.; Lu, Q. S. & Liu, Z. J. (1995). Propagation of apertured Bessel beam. *Appl. Opt.*, Vol. 34, No. 31, pp. 7183-7185

Li, S. W. & Aruga, T. (1999). Long focal depth imaging over a long range. *J. Commun. Res. Lab.*, Vol. 46, No. 3, pp. 309–310

Li, D.; Imasaki, K.; Miyamoto, S.; et al. (2006). Conceptual design of Bessel beam cavity for free-electron laser. *Int. J. Infrared Millim. Waves*, Vol. 27, No. 2, pp. 165-171

McLeod, J. H. (1954). The axicon: a new type of optical element. *J. Opt. Soc. Am*, Vol. 44, No. 8, pp. 592–597

MacDonald, R. P.; Boothroyd, S. A.; Okamoto, T.; et al. (1996). Interboard optical data distribution by Bessel beam shadowing. *Opt. Commun.*, Vol. 122, No. 4-6, pp. 169–77

Miceli J. J., Jr. & Eberly, J. H. (1988). Comparison of Bessel and Gaussian beams. *Opt. Lett.*, Vol. 13, No. 2, pp. 79-80

Monk, S.; Arlt, J.; Robertson, D. A.; et al. (1999). Generation of Bessel beams at millimetre-wave frequencies by use of an axicon. *Opt. Commun.*, Vol. 170, pp. 213-215

Meltaus, J.; Salo, J.; Noponen, E.; et al. (2003). Millimeter-wave beam shaping using holograms. *IEEE Trans. Microwave Theory Tech.*, Vol. 51, No. 4, pp.1274-1279

Mahon, R. J.; Lanigan, W.; Murphy, J. A.; et al. (2005). Novel techniques for millimeter wave imaging systems operating at 100GHz. *Proc. SPIE. Int. Soc. Opt. Eng.*, Vol. 5789, pp. 93-100

McGloin, D. & Dholakia, K. (2005). Bessel beams: diffraction in a new light. *Contemp. Phys.*, Vol. 46, No. 1, pp. 15–28

Pandit M. K. & Payne, F. P. (1997). Cerenkov second-harmonic generation by nondiffracting Bessel beams in bulk optical crystals. *Opt. Quantum Electron.*, Vol. 29, No. 1, pp. 35–51

Stratton, J. A. (1941). *Electromagnetic Theory*. McGraw-Hill, NewYork

Sprangle P. & Hafizi, B. (1991). Comment on nondiffracting beams. *Phys. Rev. Lett.*, Vol. 66, No. 6, pp. 837

Scott, G. & McArdle, N. (1992). Efficient generation of nearly diffraction-free beams using an axicon. *Opt. Eng*, Vol. 31, No. 12, pp. 2640-2643

Salo, J.; Meltaus, J.; Noponen, E.; et al. (2001). Millimetre-wave Bessel beams using computer holograms. *Electron. Lett.*, Vol. 37, No. 13, pp. 834–835

Tidwell, S. C.; Ford, D. H. & Kimura, W. D. (1992). Transporting and focusing radially polarized laser beams. *Opt. Eng.*, Vol. 31, No. 7, pp. 1527–1531

Tewari, S. P.; Huang, H. & Boyd, R. W. (1996). Theory of third-harmonic generation using Bessel beams, and self-phase-matching. *Phys. Rev. A*, Vol. 54, No. 3, pp. 2314–2325

Turunen, J.; Vasara, A. & Friberg, A. T. (1988). Holographic generation of diffraction-free beams. *Appl. Opt.*, Vol. 27, No. 19, pp. 3959–3962

Thewes, K.; Karim, M. A. & Awwal, A. A. S. (1991). Diffraction free beam generation using refracting systems. *Opt. Laser Technol.*, Vol. 23, No. 2, pp. 105–108

Trappe, N.; Mahon, R.; Lanigan, W.; et al. (2005). The quasi-optical analysis of Bessel beams in the far infrared. *Infrared Phys. Technol.*, Vol. 46, pp. 233–247

Weile, D. S. & Michielssen, E. (1997). Genetic algorithm optimization applied to electromagnetics: A review. *IEEE Trans. Antennas Propag.*, Vol. 45, No. 3, pp. 343-353

Wang, K.; Zeng, L. & Yin, Ch. (2003). Influence of the incident wave-front on intensity distribution of the nondiffracting beam used in large-scale measurement. *Opt. Commun.*, Vol. 216, No. 1–3, pp. 99–103

Yee, K. S. (1966). Numerical solution of initial boundary value problems involving Maxwell equations in isotropic media. *IEEE Trans. Antennas Propag.*, Vol. AP-14, No. 3, pp. 302-307

Yu, Y. Z. & Dou, W. B. (2008a). Scalar and vectorial properties of diffraction-free Bessel beams. *2008 Asia Pacific Microwave Conference*, APMC2008, Hongkong & Macau, China.

Yu, Y. Z. & Dou, W. B. (2008b). Vector analyses of nondiffracting Bessel beams. *Progress In Electromagnetics Research Letters*, Vol. 5, pp. 57–71

Yu, Y. Z. & Dou, W. B. (2008c). Generation of Bessel beams at mm- and submm-wave bands using binary optical elements. *2008 Global Symp. on Millimeter Waves Proc.*, Nanjing, China, pp. 115–118.

Yu, Y. Z. & Dou, W. B. (2008d). Generation of Bessel beams at mm- and sub mm-wavelengths by binary optical elements. *Int. J. Infrared Milli. Waves*, Vol. 29, No. 7, pp. 693–703

Yu, Y. Z. & Dou, W. B. (2008e). Comparison of propagation of apertured Bessel and Gaussian beams. *2008 Int. Conf. Commun. Technol. Proc.*, Hangzhou, China, pp. 217–220

Yu, Y. Z. & Dou, W. B. (2009). Generation of pseudo-Bessel beams at THz frequencies by use of binary axicons. *Opt. Express*, Vol. 17, No. 2, pp. 888-893

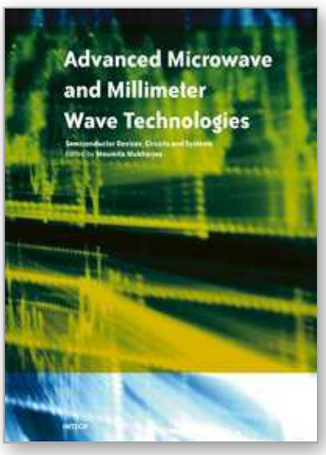

Advanced Microwave and Millimeter Wave Technologies
Semiconductor Devices Circuits and Systems
Edited by Moumita Mukherjee

ISBN 978-953-307-031-5
Hard cover, 642 pages
Publisher InTech
Published online 01, March, 2010
Published in print edition March, 2010

This book is planned to publish with an objective to provide a state-of-the-art reference book in the areas of advanced microwave, MM-Wave and THz devices, antennas and systemtechnologies for microwave communication engineers, Scientists and post-graduate students of electrical and electronics engineering, applied physicists. This reference book is a collection of 30 Chapters characterized in 3 parts: Advanced Microwave and MM-wave devices, integrated microwave and MM-wave circuits and Antennas and advanced microwave computer techniques, focusing on simulation, theories and applications. This book provides a comprehensive overview of the components and devices used in microwave and MM-Wave circuits, including microwave transmission lines, resonators, filters, ferrite devices, solid state devices, transistor oscillators and amplifiers, directional couplers, microstripeline components, microwave detectors, mixers, converters and harmonic generators, and microwave solid-state switches, phase shifters and attenuators. Several applications area also discusses here, like consumer, industrial, biomedical, and chemical applications of microwave technology. It also covers microwave instrumentation and measurement, thermodynamics, and applications in navigation and radio communication.

InTech Europe
University Campus STeP Ri
Slavka Krautzeka 83/A
51000 Rijeka, Croatia
Phone: +385 (51) 770 447
Fax: +385 (51) 686 166
www.intechopen.com

InTech China
Unit 405, Office Block, Hotel Equatorial Shanghai
No.65, Yan An Road (West), Shanghai, 200040, China
中国上海市延安西路65号上海国际贵都大饭店办公楼405单元
Phone: +86-21-62489820
Fax: +86-21-62489821

IntechOpen